nature photonics

Supplementary information

https://doi.org/10.1038/s41566-025-01651-y

Generation of ultrafast magnetic steps for coherent control

In the format provided by the authors and unedited

S1. Ultrafast Magnetometry Technique

Ultrafast optical magnetometry relies on the Faraday effect, which directly relates the magnetic field applied to a material to the polarization rotation of a linearly polarized beam traversing the medium. This relation is usually reported as:

$$\theta = V \cdot \int_0^L B(z)dz \qquad \text{(Eq. S1)}$$

where θ represents the rotation of the polarization of the input beam, B(z) is the magnitude of the magnetic field along the light propagation direction inside the medium, and L is the thickness of the medium. The proportionality constant V is known as the Verdet constant, which is a material-dependent constant that also depends on other parameters such as the wavelength of the incoming polarized light. This expression highlights the fact that the magnetic field is averaged across the thickness of the material traversed. Therefore, if B varies strongly over distances of order ~L, its spatial dependence is blurred in the accumulated polarization rotation.

In the past, the Faraday effect in ferromagnetic crystals and thin films has been used to image the magnetic properties of superconductors at equilibrium[1,2]. These types of detectors (such as Bi:$R_3Fe_5O_{12}$, EuS, and EuSe) offer very high sensitivity (V~10^5 rad·T^{-1}·m^{-1}) but have limited time resolution, down to 100 ps at best, due to the presence of low-lying magnetic excitations (e.g., ferromagnetic resonance) at sub-THz frequencies. On the other hand, diamagnetic II-VI and III-V semiconductors such as ZnSe, ZnTe, and GaP have a magneto-optic response featuring Verdet constants that are two to three orders of magnitude smaller than those observed in ferromagnetic materials but have the advantage of not being magnetically ordered and offer significantly better time resolution[3,4]. Furthermore, their Verdet constant is mostly temperature-independent, ensuring a flat detector response in a broad temperature range.

The measurements shown throughout the manuscript were performed using GaP and $Lu_2Bi_1Fe_4Ga_1O_{12}$ (Bi:LIGG) magneto-optic crystals. Their sensitivity to magnetic fields was calibrated before each measurement in the exact experimental conditions used for the measurement. We measured the amount of angular polarization rotation in a position of GaP or Bi:LIGG far from the sample (see Fig. 1 of the Main Text), where the magnetic field was equal to the uniform externally applied magnetic field. In this way, we could extract a calibration factor specific to our experimental conditions, which allowed us to convert the measured polarization rotation into the value of the local magnetic field in the crystal.

Finally, to have an accurate calibration of the actual value of the magnetic field, the current-to-magnetic field constant of the Helmholtz coil pair was independently calibrated in situ using a Lakeshore 425 gaussmeter. These calibration measurements yielded a Verdet constant of ~120 rad·T^{-1}·m^{-1} for GaP, after accounting for the magneto-optic crystal thickness, in agreement with reported literature values[5], and of ~$0.5 \cdot 10^5$ rad·T^{-1}·m^{-1} for Bi:LIGG, in agreement with the values specified by the company producing the samples (see Supplementary Information S2).

S2. Sample Characterization

The optimally doped $YBa_2Cu_3O_7$ thin films were obtained through a commercial supplier (Ceraco GmbH) and grown on r-cut Al_2O_3 substrates. We chose the S-Type films, with a thickness of approximately 150 nm, critical current density greater than 2 MA/cm^2, and specified T_c of 86 K. The superconducting transition temperature of the device after lithography (see Supplementary Information S3) was 85 K (see Fig. 1b of the Main Text). The slight copper excess used by the manufacturer to optimize the superconducting properties of the sample results in small copper-oxide precipitates on the surface of the YBCO film.

The ~3μm thick Bi-substituted lutetium iron gallium garnet ($Lu_2Bi_1Fe_4Ga_1O_{12}$, Bi:LIGG for short in the following) sample was obtained through a commercial supplier and grown by Liquid-Phase Epitaxy on a (100)-oriented, 500 μm thick $Gd_3Ga_5O_{12}$ crystal (GGG). The composition of the Bi:LIGG sample was measured using energy-dispersive X-ray spectroscopy (EDX) yielding the following percentage composition of elements: O 58.98%, Fe 19.43%, Ga 5.99%, Lu 10.28%, Bi 5.32%. This result is in good agreement with the chemical formula reported above.

S3. Sample preparation and Experimental Geometries

A 150 nm-thick $YBa_2Cu_3O_7$ film grown on a two-side polished Al_2O_3 substrate was patterned into a disc shape using a laser lithography process based on an AZ1512 photoresist mask. After exposure and development, the sample was wet etched using a 1% H_3PO_4 solution. After etching, the residual photoresist was removed using acetone and isopropanol. Fig. S3a shows a micrograph of the $YBa_2Cu_3O_7$ film after patterning. The thin film and GaP (100) detector were then mounted onto an Al_2O_3 plate that could be fixed directly to the cold finger of the cryostat. Al_2O_3 is an electrical insulator that minimizes magnetic field

shielding due to eddy currents while ensuring good cooling power. A 75 µm thick GaP (100) crystal (SurfaceNet GmbH) was used as a detector and put in close contact with the sample (see Fig. S3b). The detector was polished with a wedge angle of ~1.5° to spatially separate the reflections from the front and back surfaces. This precaution allowed us to detect exclusively the reflection from the back surface, which accumulated the Faraday polarization rotation signal as the probe beam propagated across the detector thickness. Additionally, the GaP back surface and the sample were not coplanar to avoid interference between the reflections from these two surfaces (see Fig. S3c). The gap between the detector and the $YBa_2Cu_3O_7$ disc was ~25 µm. This experimental geometry was used for the measurements shown in Figs. 1 and 2 of the Main Text. For those reported in Fig. 3, the GaP detector was directly replaced by the ferrimagnetic Bi-substituted rare earth iron garnet sample. The surface of the sample exposing the ferrimagnetic layer was placed close to the $YBCO_7$ disc, and the wedge, in this case, was polished on the GGG substrate facing the incoming probe beam.

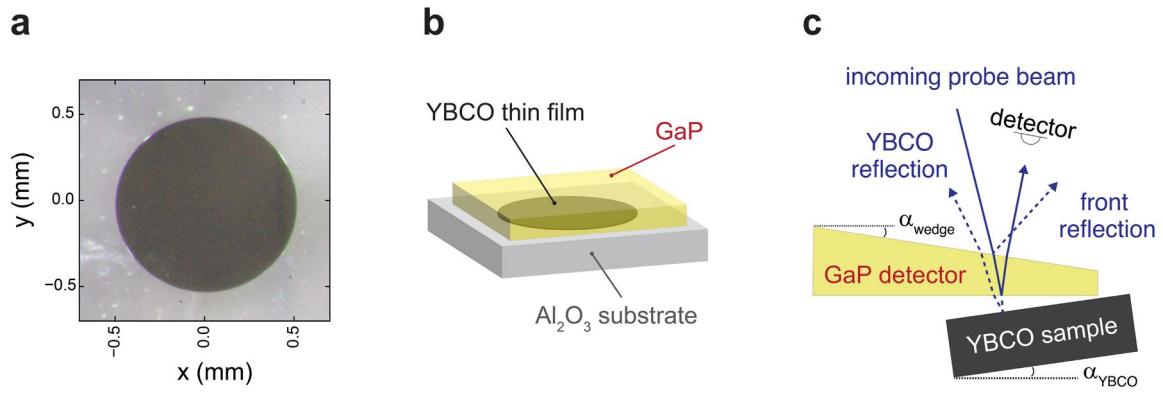

Figure S3. | **(a)** Micrograph of the $YBa_2Cu_3O_7$ thin film patterned into a 1 mm diameter disc shape. **(b)** Sketch of the sample configuration highlighting the positioning of the GaP (100) magneto-optic detector on the $YBa_2Cu_3O_7$ disc. **(c)** Side view highlighting how undesired reflections are filtered out. The GaP detection crystal is wedged to spatially separate the front and back reflections from each other. The YBCO sample is then mounted with a slight tilt compared to the detector's back side. This angle is big enough to filter out the reflection from the YBCO surface but small enough not to interfere with the measurement. Both angles are exaggerated for clarity; in reality, α_{wedge} ~1.5° and α_{YBCO} ~1°.

S4. Experimental Setup and Data Acquisition

The measurements were performed using the experimental setup sketched in Fig. S4. Ultrashort (100 fs) 800 nm center wavelength laser pulses were produced starting from a

commercial $Ti:Al_2O_3$ oscillator/amplifier system that produced pulses with energies of 2 mJ at a repetition rate of 900 Hz. These pulses were split using a beamsplitter into two branches. After attenuation, the lowest intensity branch was used for probing Faraday rotation in the GaP (100) detector and Bi:LIGG samples. The polarization of the beam was set using a nanoparticle high-extinction ratio linear polarizer to minimize the noise sources in the measurement.

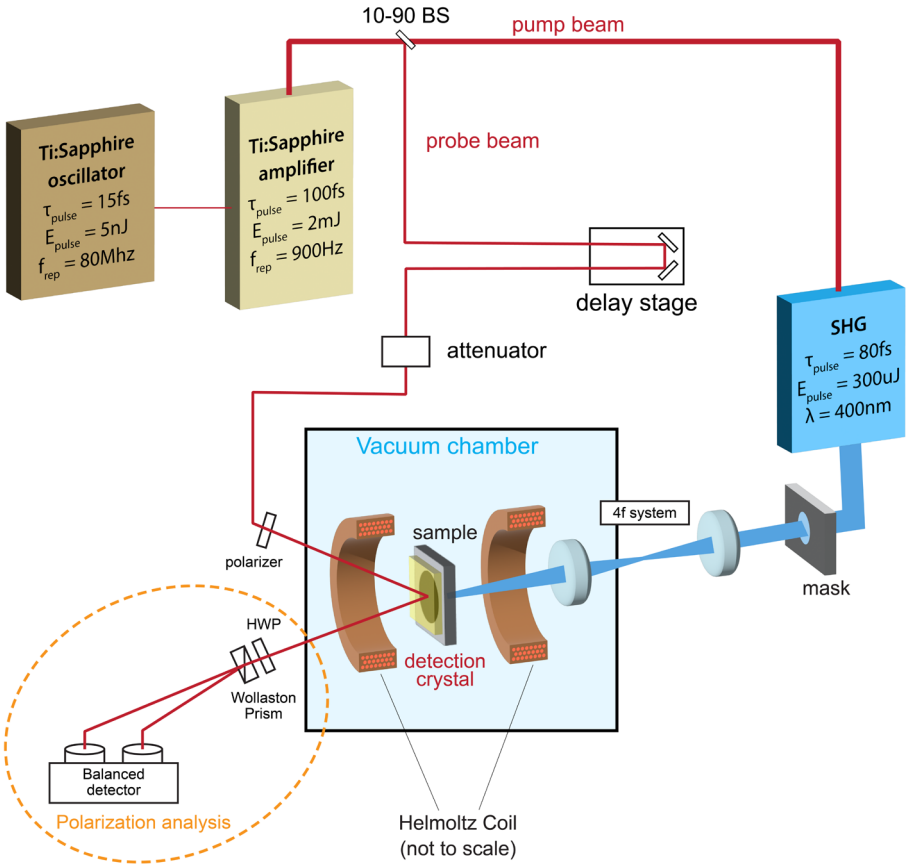

Figure S4. | Experimental setup.

As non-normal incidence reflections introduce a phase delay between *s* and *p* polarization, incidence angle fluctuations can give rise to polarization noise. Only reflections close to normal incidence were used in the setup to minimize the effect of angular fluctuations, and a commercial system using active feedback was used to stabilize the laser beam pointing. After traversing and being reflected from the second surface of the Faraday detector, the polarization state of light was analyzed using a half-waveplate, Wollaston prism, and balanced photo-diode setup that allowed us to quantify the Faraday effect in the magneto-optic detection crystal. The higher intensity branch was frequency doubled using a β-BaB_2O_4 crystal to obtain 400 nm pulses to photo-excite the $YBa_2Cu_3O_7$ thin film sample. A mask, illuminated by these ultraviolet pulses, was imaged onto the back surface of the

sample to create a flat top, disc-shaped beam that matched precisely the size of the disc-shaped $YBa_2Cu_3O_7$ (see Supplementary Information S11). This precaution and the $YBa_2Cu_3O_7$ being opaque to 400 nm radiation ensured that the GaP detector was not exposed to the pump pulses.

The $YBa_2Cu_3O_7$ thin film samples were embedded in the detector assembly (Fig. S3) and mounted on the cold finger of a liquid helium cryostat to allow for temperature control. The cryostat was directly placed in a high vacuum chamber. A pair of coils in a Helmholtz configuration generated a magnetic field at the sample position whose polarity could be reversed at a frequency of 450 Hz. Switching the polarity of the magnetic field helped reject possible spurious contributions (see Supplementary Information S5) arising from unwanted sources of bi-refringence (e.g., residual strain in the detector crystals or vacuum windows). The highest achievable magnetic field was limited by heat dissipation and was ~3 mT. The sample position was changed using computer-controlled linear translation stages that made it possible to reproducibly move the cryostat and the sample inside the vacuum chamber with ~10 μm repeatability.

The electrical pulses from the balanced photodetector were digitized using a commercial 8-channel 40MS/s data acquisition card triggered at the lowest frequency used in the experiment to obtain differential magnetic field measurements. These pulses, acquired in the time domain, were then integrated by applying a boxcar function to yield the signals from the sum and difference channels of the balanced photodetector for each probe laser pulse (see Fig. S5 in the following section). Since acquiring a complete pulse sequence required the acquisition of many cycles of the applied magnetic field, the sample clock signal of the data acquisition card was derived using direct digital synthesis from the oscillator repetition rate. In this way, drifts in the cavity length and repetition rates of the system did not affect the relative timing of the boxcar functions compared to the arrival time of the electrical signal from the photodiodes.

S5. Data Reduction and Analysis

As mentioned in the previous section, the polarity of the magnetic field was cycled periodically to yield differential measurements and isolate contributions to the polarization rotation that were only induced by the applied magnetic field. In other words, because the equilibrium and pump-induced magnetic field changes measured with applied field $-H_{app}$ were subtracted from those acquired with applied field $+H_{app}$, the sensitivity of the signal

to strain in the magneto-optic detector or polarization noise in the setup was strongly reduced. In the following paragraph, we discuss this approach in detail.

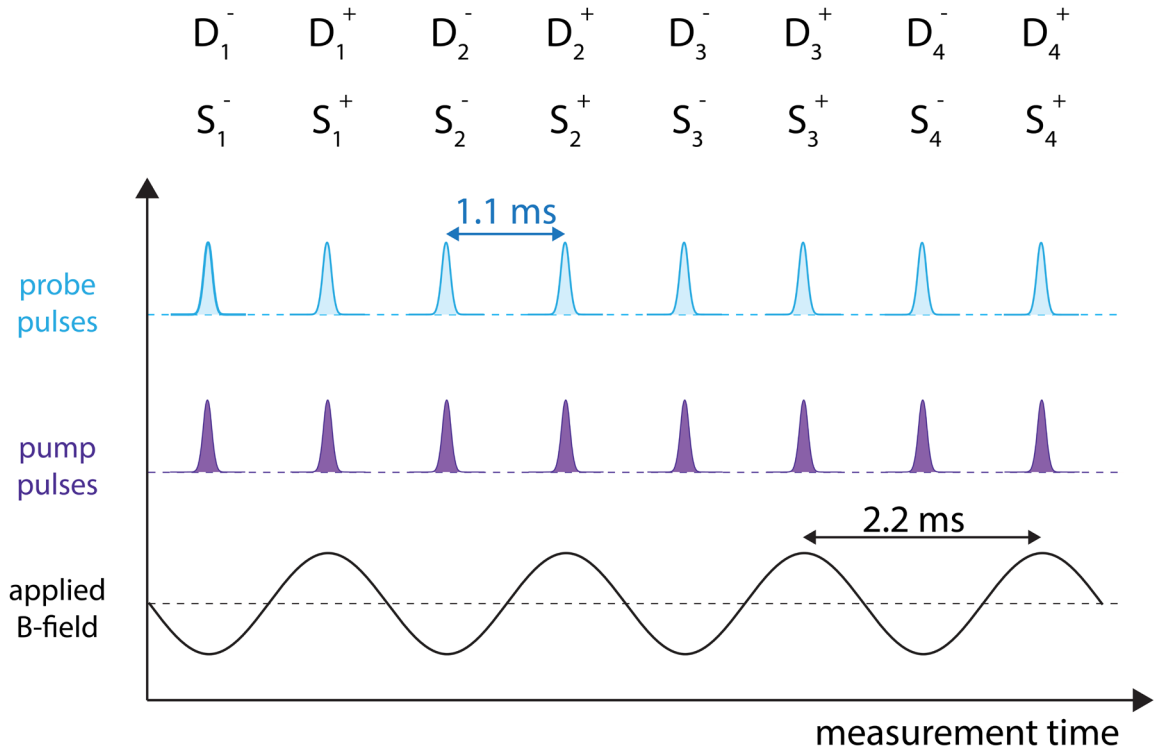

Figure S5. | Timing diagram of the acquisition scheme used for the measurements shown in the Main Text. We indicate the signals from the difference and sum channels of the photodetector with D and S, respectively.

The magnetic field polarity was cycled following a sinewave at 450 Hz frequency. We chose the highest possible switching frequency to reject low-frequency 1/f noise efficiently. A timing diagram of the acquisition scheme is shown in Fig. S5. As mentioned in section S4, we triggered the data acquisition card at a sub-harmonic frequency of the probe repetition rate corresponding to traces comprising 88 pulses (a trace of 8 pulses is shown in Fig. S5 as an example). In the end, only 80 of these 88 pulses were acquired due to a fixed dead time for data processing.

We label signals from the difference and sum channels of the photodetector as $D_i^{\pm}$ and $S_i^{\pm}$ respectively to indicate whether they were acquired with positive (+) or negative (-) polarities of the applied magnetic field. The subscript i runs over the 80 acquired pulses in the acquisition trace. The polarization rotation within a trace is calculated in the following way:

$$\Delta\vartheta = \frac{\sum_i^{80} D_i^+}{\sum_i^{80} S_i^+} - \frac{\sum_i^{80} D_i^-}{\sum_i^{80} S_i^-}. \qquad \text{(Eq. S5)}$$

This quantity yielded the amplitude of the magnetic field after calibration of the Faraday effect in the GaP (100) detector and Bi:LIGG sample (see Supplementary Information S1). To limit computational dead times between acquisitions, we normalize after averaging as indicated in the formula above.

The sequential acquisition of multiple pulses (88) allowed us to minimize the impact of lost pulses during processing time while keeping the frequency of acquisition as high as possible to reject the effect of low-frequency noise when averaging the difference and sum channels within a trace before taking the ratio of the two quantities. The phase of the sinusoidal magnetic field applied was periodically alternated between 0 and π compared to the laser pulse train to cancel out residual drifts due to possible asymmetries in the applied magnetic field.

During the pump-probe measurements, each probe signal was acquired while the optical pump was on (see Fig. S5). This approach was convenient for reducing asymmetries due to the long-lasting heating effect in the superconducting film (see Supplementary Information S14). The magnetic dynamics induced by the pump were then measured by changing the value of the probe arrival time relative to the pump.

S6. Shielding of Time-varying Magnetic Fields in Superconductors

When a superconductor is cooled below T_c and a time-varying magnetic field is applied, magnetic field exclusion occurs (see Fig. S10.3a). This phenomenon is due to the perfect conductivity of the $YBa_2Cu_3O_7$ sample below T_c. Magnetically induced persistent shielding currents keep the magnetic flux constant in the superconductor, as Faraday-Lenz law prescribes. The magnetic field is completely excluded from the sample volume, even if defects exist, unlike what happens for the Meissner effect (see Supplementary Information S7). This response is observed in zero-field cooled experiments[6,7].

Fig. S6 qualitatively explains the equilibrium field dynamics in our experiment, which is very similar to the zero-field cooled regime. Fig. S6a shows the temperature evolution during a hypothetical experiment in which a sample is progressively cooled below T_c. Fig. S6b shows the probe pulses used to sample the magnetic field at a specific point in time. When there is no sample, we expect to measure a value equal to the amplitude of the applied sinusoidal magnetic field. The temperature dependence of the GaP detector is weak, so we do not see any change in the response when cooling (see Fig. S6c). As described in Supplementary Information S5, the magnetic field is extracted as the difference between

the polarization rotation measured when the polarity of the sinusoidal wave is positive minus the one measured when the polarity is negative. Fig. S6d schematically shows the evolution of the magnetic field upon cooling our sample across T_c. Initially, when the sample is above T_c, the magnetic field measured is almost equal to the applied magnetic field due to the higher resistivity of the thin film in the normal state. As described above, the superconductor begins to partially shield the time-varying applied field after cooling across T_c. In this temperature regime close to T_c, the shielding is incomplete due to residual dissipation and the superconductor low critical current density. Upon further cooling, the shielding improves as the superfluid density increases, and the superconductor behaves like a perfect metal in which the eddy currents induced by the applied field become persistent due to the absence of dissipation. In this regime of perfect screening, the field on top of the sample is constant. Our differential measurement yields a value of the magnetic field close to zero above the center of the superconductor, as shown on the left side of Fig. 1b in the Main Text.

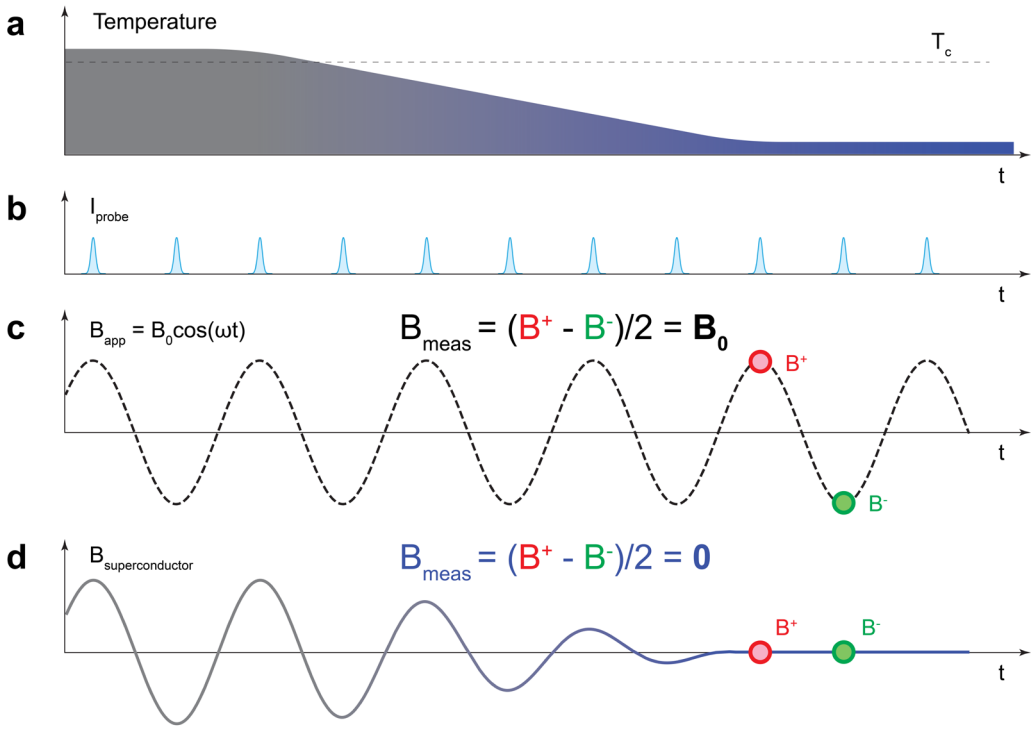

Figure S6. | **(a)** Sketch of the temporal profile of the temperature when cooling the sample below T_c. **(b)** Arrival time of the probe pulses sampling the magnetic field. **(c)** Externally applied magnetic field with a sinusoidal time evolution. **(d)** Magnetic shielding of the superconductor when cooling across T_c.

S7. Field Cooled vs. Zero-Field Cooled Magnetization

The magnetic field measured in our experiment originates from changes in the magnetization of $YBa_2Cu_3O_7$, which can occur through two mechanisms: magnetic field expulsion, the response of a superconductor to static magnetic fields, or magnetic field exclusion, its response to time-varying magnetic fields. These scenarios correspond to the well-known Field-Cooled (FC) and Zero-Field-Cooled (ZFC) measurement protocols, respectively.

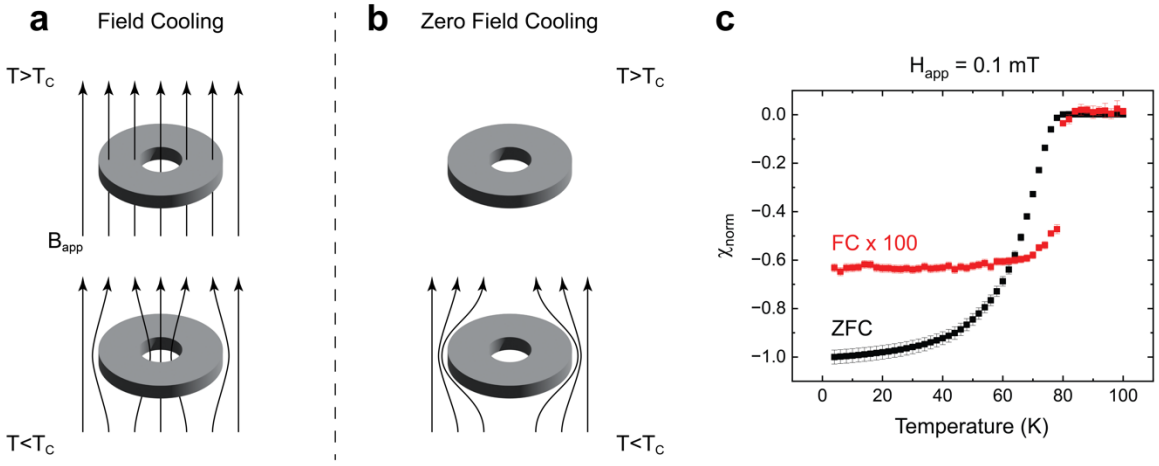

Figure S7.1. Sketch representing how an applied magnetic field is modified by a superconducting sample with a hole, representing a non-superconducting defect. **(a)** When the sample is cooled in a magnetic field, the field is expelled from the sample and trapped into the hole, reducing the net magnetization of the sample compared to a defect-free sample. **(b)** When the sample is first cooled below T_c, and then a magnetic field is applied, the field is excluded from the whole sample volume, no matter the presence of defects. **(c)** SQuID magnetometry data measured on a $YBa_2Cu_3O_7$ film analogous to those used in this work. The magnetic was applied along the $YBa_2Cu_3O_7$ c-axis. Each data point represents the mean value ± s.e.m. extracted from a sample of 600 measurements.

In a defect-free superconductor, both phenomena would result in perfect magnetic field shielding below the critical field. However, as schematically shown in Fig. S7.1, the presence of defects (depicted as a hole in the superconducting disc) alters this behavior. In the field-cooled scenario, the Meissner effect expels the magnetic field only from the bulk of the superconductor, leaving it trapped in the hole and leading to reduced magnetization[6,7]. In contrast, zero-field-cooled measurements still exhibit full magnetic field exclusion due to the sample perfect conductivity. To quantify this difference for the $YBa_2Cu_3O_7$ thin film used in this work, we performed ZFC and FC SQuID magnetometry measurements. The results (Figure S7.1c) reveal that the FC response is over two orders of magnitude smaller than the ZFC response. This finding justifies our choice of resorting to zero-

field cooled protocol in our measurements (see Supplementary Information S6) to maximize the superconductor's diamagnetic response and decrease the impact from the presence of defects.

Field Cooled Magnetisation Modelling

We used magnetostatic calculations to assess the effect of flux-trapping defects on the Meissner response in our experimental geometry. We modeled the superconducting thin film as a uniform medium with a magnetic permittivity close to zero. The presence of defect was simulated by introducing gaps (width of 150 nm) in the sample spaced 10 µm from each other. The changes in the magnetic field surrounding the sample were calculated using COMSOL Multiphysics to solve Maxwell's equations.

We calculated the measured magnetic signal in our geometry by integrating the z-component of the magnetic field in the volume of the GaP detector traversed by the probe. This calculation has been done in two steps, first by integrating along the thickness (75 um) of the detector and then by convoluting the result with a Gaussian envelope representing the probe spot size (50 µm FWHM). The results of this calculation are shown in Fig. S7.2b. The presence of discontinuities, mimicking the effects of defects, strongly reduces the field-cooled magnetic response in our configuration and is not spatially resolved, due to the spatial average across the thickness of the GaP detector and to the smoothing effect from the finite size of the probe pulse.

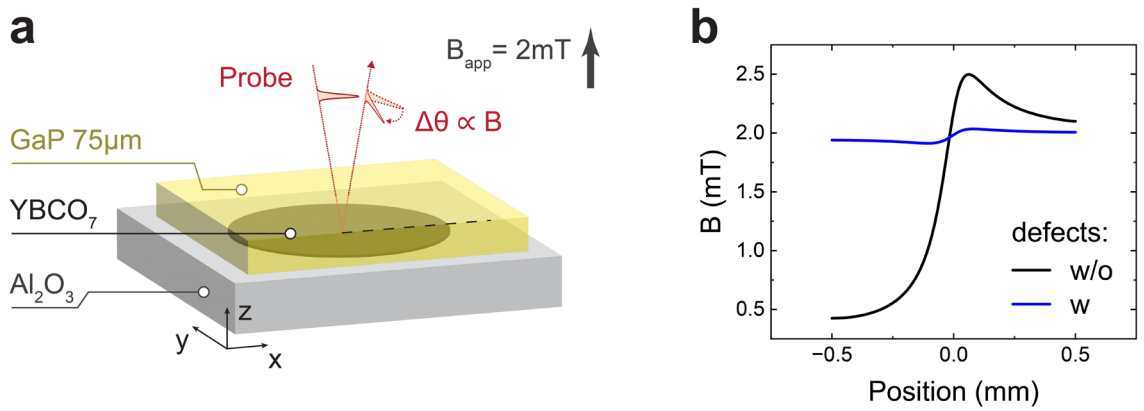

Figure S7.2. | **(a)** Geometry of the experiment. The black dashed line represents the direction of the spatial scan shown in b. **(b)** Simulated magnetic field spatial dependence across the edge of a perfectly diamagnetic thin disc with a radius of 500 µm in a 2 mT externally applied field, with ("w") and without ("w/o") non-superconducting defects measured in GaP.

Zero-field Cooled Magnetisation Modelling

In our experiment, switching the polarity of the external magnetic field generates shielding currents in $YBa_2Cu_3O_7$, producing a zero-field-cooled like response (see Supplementary Information S6). We simulated this phenomenon with finite element calculations using COMSOL Multiphysics in a 3D geometry with axial symmetry.

The changes in the magnetic field surrounding the sample were calculated, taking into account the geometry of the experiment. The solution domain was defined as a cylindrical region with a radius and a height of 1 mm. The $YBa_2Cu_3O_7$ sample was modeled as a disc with a radius of 500 μm and a thickness of 150 nm with a high conductivity (10^{11} S/m). The magnetic field shielding from the superconductor (discussed qualitatively in Supplementary Information S6) was modeled by ramping up a uniform applied magnetic field from 0 to 2 mT in 1 ns along the direction perpendicular to the plane of the disc. The magnetically induced eddy currents in the simulation reproduced the effect of the superconducting screening currents measured in the experiment, having the same physical origin: Faraday law. On these short time scales, the decay of the eddy currents was negligible (due to the high conductivity of the sample), and the magnetic shielding was constant, as expected from superconducting persistent currents. The substrate of the $YBa_2Cu_3O_7$ was not included in the modeling due to its much lower conductivity. Furthermore, we did not include effects due to the finite critical current of the sample since the magnetic field applied in the experiment (2mT) was always lower than the first critical field of YBCO (~100 mT[8]). Even considering demagnetizing effects appropriate for our geometry, we expect to reach the critical current threshold only in a small region close to the edge of the disc[9,10]. Therefore, our simulation matches our experimental conditions well and agrees with the experimental results (see Supplementary Information S8). The simulations reported in Fig. 1 of the Main Text have been achieved with this method.

S8. Additional spatial dependencies at equilibrium

The data points in Fig. S8a-b show respectively the z component of the magnetic field measured in the GaP and in the Bi:LIGG detectors as a function of the distance from the center of the $YBa_2Cu_3O_7$ disc, which is kept below T_c. The data clearly show a spatially dependent shielding of the applied magnetic field. We simulate this shielding with the zero-field cooled method described in Supplementary Information S7, first calculating the equilibrium magnetic field distribution in space generated by the $YBa_2Cu_3O_7$ sample (Fig.

S10.3a) and then convoluting the averaged magnetic field across the thickness of each detector with a Gaussian profile (50 μm FWHM) representing the probe beam. The distance of the detector from the superconductor used in the simulations is 45 μm for the GaP and 5 μm for the Bi:LIGG. Both these values are compatible with the geometry of the experiment. The dotted curves in Fig. S8 show the results of this simulation, which are in good agreement with the experimental data.

By comparing measured data and simulations, we conclude that the spatial resolution of the GaP detector is limited by its thickness (75 μm). Conversely, for the Bi:LIGG detector the probe size (50 μm FWHM) is the limiting factor. This result can be understood by an additional comparison of the data to simulations carried out assuming a point-like probe beam (not shown). For the GaP, the agreement between the two is unchanged, while for the Bi:LIGG, the simulated spatial features are sharper than the measured ones. Owing to its higher resolution, the Bi:LIGG detector measures an enhancement of the magnetic field at the edge of the superconductor which is much larger than that measured by the GaP.

Due to the higher spatial resolution, measurements performed with Bi:LIGG allow us to put an upper limit to the region in the sample where the critical current is reached as the magnetic field can penetrate in those areas[9,11]. From Fig. S8b below, we can see that the externally applied magnetic field is completely shielded less than 150 μm away from the edge of the sample. 100 μm is an upper limit, given that we do not correct for the finite size of the probe spot, which blurs the spatial resolution. This result justifies the approximated model, which does not consider the effect of critical currents, employed here and in Supplementary Information S7 and S10 to simulate the superconducting shielding.

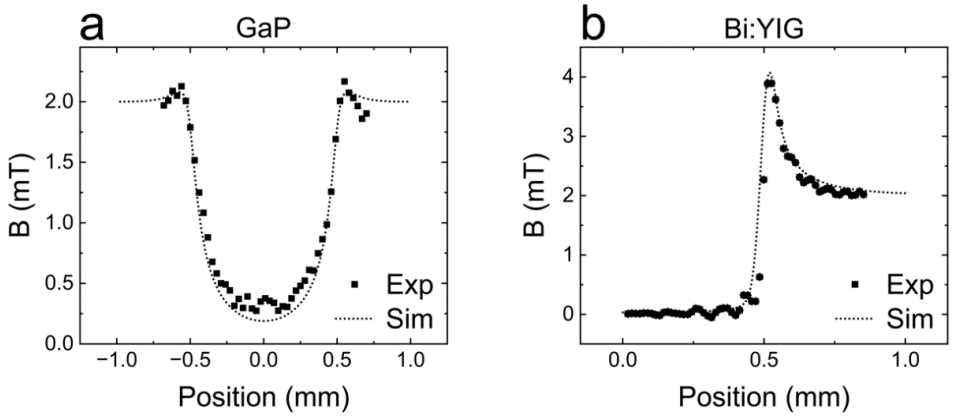

Figure S8. | Measured (datapoints) and simulated (dotted lines) z component of the magnetic field measured while scanning the position of the probe beam across the $YBa_2Cu_3O_7$ disc with **(a)** the GaP detector and **(b)** the Bi:LIGG sample. Due to averaging effects through its thickness, the measured magnetic field exclusion in GaP is reduced. Each data point in **(b)** represents mean value ± s.e.m. (smaller than the size of the data points) extracted from a sample of 16 acquisitions.

S9. Mechanisms for Optical Disruption of Superconductivity

In this section, we discuss the well-established microscopic mechanisms by which an optical pump pulse disrupts superconductivity in high-Tc cuprates[12–14]. In general, this obtained by irradiating the samples with near-infrared or visible pulses that excite electronic transitions generating, an increase of quasi-particles at the expense of the superconducting condensate on ultrafast time scales.

Averitt et al.[12] measured the ultrafast (ab)-plane dynamics of quasiparticles and superconducting pairs in $YBa_2Cu_3O_7$ thin films using optical-pump terahertz-probe spectroscopy in a wide temperature range. After optical excitation with a 150 fs, 1.5 eV pulse, they measured a substantial decrease in imaginary part of the optical conductivity and an increase in the real part. This observation is interpreted as a decrease in the superconducting carrier fraction, which partially recovers on picosecond time scales. Importantly, the recovery of the system to the equilibrium superconducting state was incomplete also at time delays up to a few ns, due to the presence of high-energy phonons. These high-energy phonons (with energy larger than $2\Delta \sim 100$ meV) can provide energy to break Cooper pairs and generate quasiparticles up to ns time scales[15]. These are the time scales the film needs to return to the initial state as the phonons with energy higher than 2Δ are absorbed by the substrate via thermal transport. These findings agree with those from Kaindl et al. [13] and Pashkin et al.[14] who performed similar measurements in the mid-infrared range on optimally doped $YBa_2Cu_3O_7$ thin films. They found that the the equilibrium superconducting gap fills on ultrafast time scales and recovers in a few picoseconds.

The disruption timescales observed with THz and mid-infrared spectroscopy are one order of magnitude faster than the magnetic dynamics we observe, which are instead governed by extrinsic factors - specifically, the total inductive response of $YBa_2Cu_3O_7$ in the quenched state and its conductivity (see Supplementary Information S10).

Moreover, our measurements are fully compatible with these recovery times. As detailed in Supplementary Information S7, the measured magnetic field originates from changes in the magnetization of $YBa_2Cu_3O_7$, which can occur through two mechanisms: magnetic field expulsion, the response of a superconductor to static magnetic fields (field cooling), or magnetic field exclusion, its response to time-varying magnetic fields (zero-field cooling). In our experiment, switching the polarity of the external magnetic field generates shielding currents in $YBa_2Cu_3O_7$, producing a zero-field-cooled like response. Optical excitation disrupts superconductivity and magnetic field exclusion on sub-picosecond time-

scales, creating an ultrafast magnetic step. $YBa_2Cu_3O_7$ then recovers in the applied magnetic field over a few picoseconds. Given that this process occurs 11-12 orders of magnitude faster than the field polarity switching (~1 ms), the magnetic field during recovery remains constant. As a result, the recovery signal reflects only the field-cooled response, which is over two orders of magnitude smaller than the ZFC-like transient and is not observed in the measurement (see also Supplementary Information S14 for more details).

S10. Modeling the Ultrafast Magnetic Step

To gain deeper insight into the ultrafast magnetic field steps dynamics, we modelled our device with a simple circuit model characterized by an inductor (with inductance L) and a resistor (with resistance R). This model aims to describe the decay of the shielding currents as superconductivity is disrupted in the sample by the optical pulse. Indeed, the data shown in Fig. 2 of the Main Text can be fitted well by a single exponential decay function of the form (see Fig. S10.1):

$$y(t) = \begin{cases} y_0\,, & t < t_0 \\ y_0 + A \cdot \left(1 - e^{-\frac{t-t_0}{\tau}}\right), & t \geq t_0 \end{cases} \qquad \text{(Eq. S10)}$$

representing the typical response to a voltage step of an L/R circuit.

In this formula: t is the independent variable representing the time delay, y_0 is the baseline at negative time delays accounting for the magnetic flux trapped at $t<t_0$, A is the amplitude of the magnetic step, t_0 is the arrival time of the quench beam and τ is the characteristic rise-time of the magnetic step. The value of ΔB shown in Fig. S10.1 is achieved by subtracting the fitted value of y_0 from the measured magnetic field. The value of τ extracted from the fit is roughly 1.3 ps. In this picture, the quench pulse creates a sudden increase in the resistivity of the disc, with the current decreasing on time scales dictated by the inductance and resistance of the photo-excited state. We estimated the L/R time constant in our geometry to more quantitatively validate this simple circuit model.

We used COMSOL to extract the effective esistance and inductance of a thin disk with a conductivity of 10^6 S/m, a value similar to the normal state in-plane conductivity of YBCO at 100K[16]. We take into account that the current mainly flows at the edges of the disc[11] by modeling our sample as a ring with an internal radius equal to 70% of the external radius and biasing it with a uniform current distribution to extract L and R. Fig. S10.2 shows the linear dependence of the time constant of the system (equal to L/R) as a function of the

external radius *r* of the ring. When *r* is set to 500 μm, the time constant extracted is 9.2 ps. This value is roughly 7 times bigger than what was measured in the experiment (~1.3 ps).

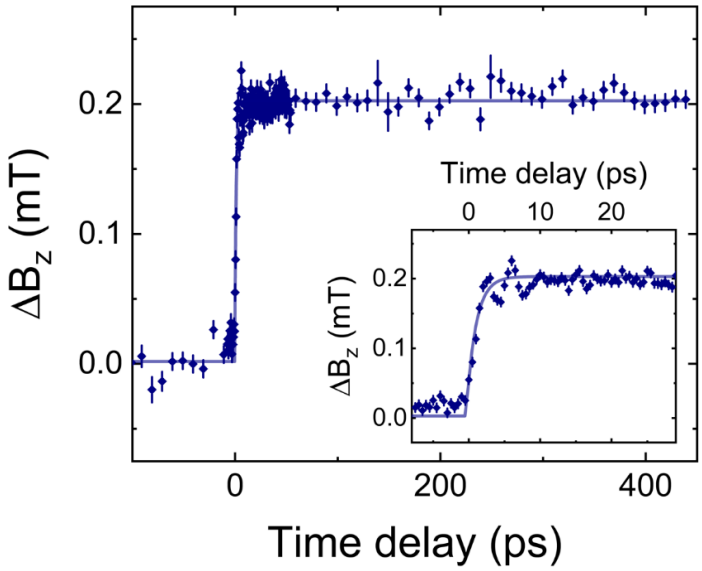

Figure S10.1. | Fit of the quench-induced changes in the *z*-component of the local magnetic field, ΔB_z, measured above the centre of the disc as a function of pump-probe delay. The diamonds represent experimental data points; the solid line is the fit with a rise and single-time constant exponential decay (see above). The inset shows a zoom-in at short time delays around time zero. The value of the measured magnetic field at negative time delays is equal to 0.45 mT due to the trapped flux in the superconductor between consecutive pump pulses (see Supplementary Information S14). Each data point represents the mean value ± s.e.m. extracted from a sample of 1100 acquisitions (Supplementary Information S5).

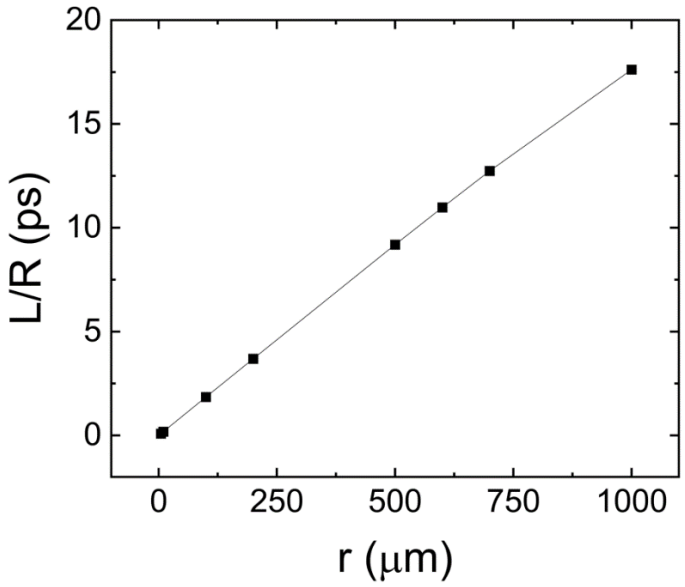

Figure S10.2. | Simulated time constant (L/R) of a resistive ring with conductivity 1 MS/m, thickness 150 nm, and ratio internal to external radius fixed to 0.7 versus the size of the external radius *r*.

The most significant uncertainty in our model comes from the value used for the conductivity of the photo-excited state. Another factor that makes this estimate only partially accurate is that we use a uniform current distribution to bias the sample, not the actual spatial distribution of the current in the sample before the quench beam hits it. These two aspects can explain the discrepancy between experiments and simulations. Although not perfectly correct, this model still has the advantage of being simple and highlighting that reducing the diameter of the superconducting disc is the path forward to achieve faster switching times.

To refine the modeling of the dynamics of the magnetic step, we performed a time-dependent finite element calculation using COMSOL Multiphysics. The framework is similar to the one used in Supplementary Information S7 to describe zero-field cooled shielding currents, to which a sudden change in conductivity was added to reproduce the effect of the quench pulse. To limit the computational cost needed for this modelling, the solution domain was smaller than the actual experiment and was defined as a cylindrical region with a radius and a height of 10 µm. The $YBa_2Cu_3O_7$ sample was modeled as a disc with a radius of 5 µm and a thickness of 150 nm with a high conductivity (10^{11} S/m). The initial state before photo-excitation (magnetic field exclusion) was obtained by ramping up a uniform applied magnetic field from 0 to 2 mT in 1 ns along the direction perpendicular to the plane of the disc. We then simulated the ultrafast magnetic step by quenching the conductivity of the thin disc to 10^6 S/m, which is the conductivity assumed above for the photo-excited state. This assumption is equivalent to stating that the pump pulse turns all the superconducting carriers into normal carriers.

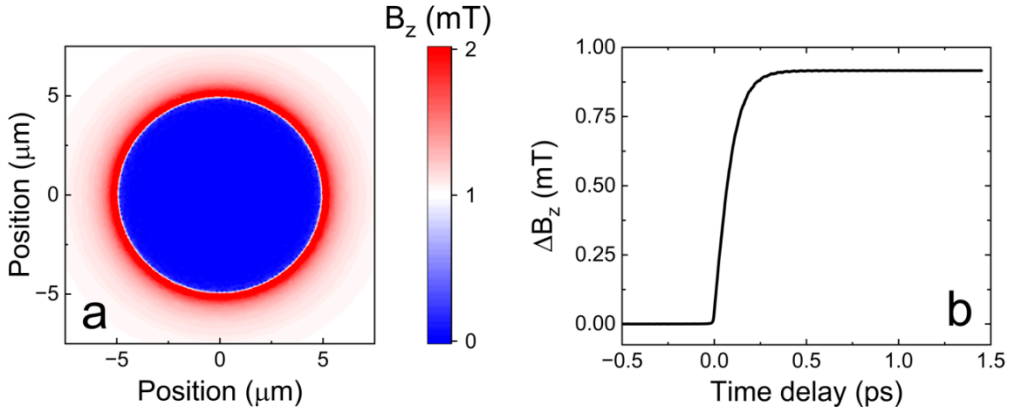

Figure S10.3. | **(a)** Simulated z component of the magnetic field (B_z) above the centre of the superconductor at negative time delays. **(b)** Change of B_z in time after the conductivity quench.

The results we achieved are shown in Fig. S10.3. Before the quench of the conductivity, the equilibrium distribution of the magnetic field (Fig. S10.3a) is qualitatively similar to

what is reported in Fig. 2 of the Main Text. Fig. S10.3b shows the magnetic field dynamics in the disc center after the conductivity quench. The shielding disappears on ultrafast time scales and after roughly 0.3 ps, the magnetic field reaches the value of the applied field. A single exponential fit (see equation above) accurately captures the time dependence shown in Fig. S10.3b, resulting from this simulation. This fit yields a time constant of ~ 0.08 ps, which agrees with the L/R time constant of 0.088 ps calculated above when setting r to 5 μm (see Fig. S10.2). This result further validates the simple circuit model we used above and its predictive value.

S11. Imaging System

Fig. S11 shows a schematic representation of the imaging setup used to excite the superconducting $YBa_2Cu_3O_7$ disc with a flat top beam matching its shape.

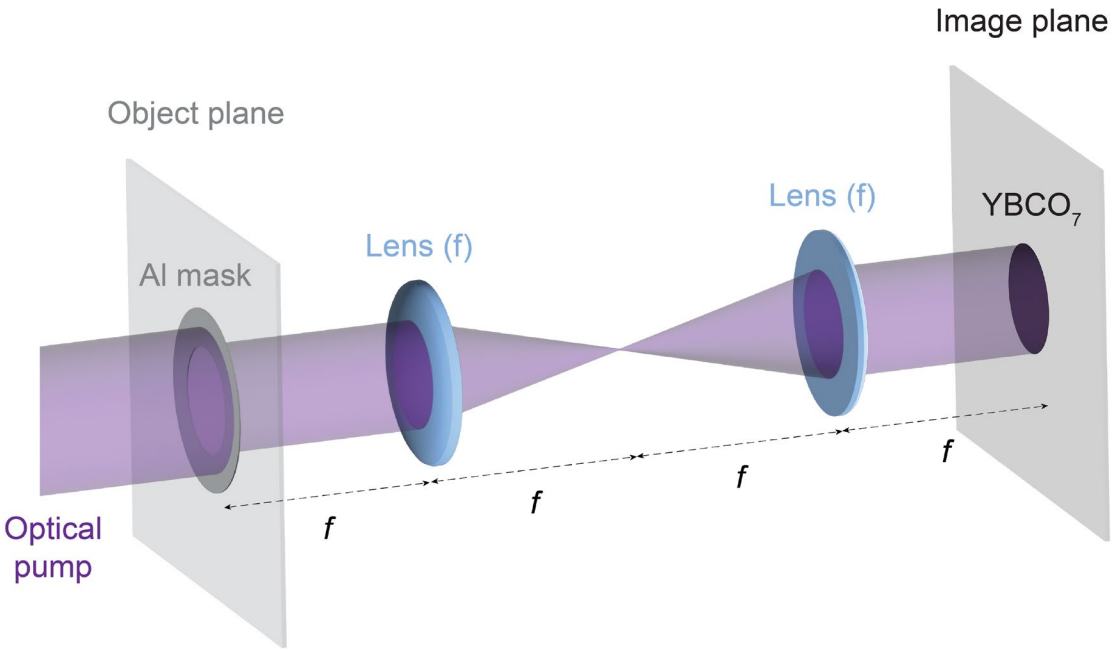

Figure S11. | Schematic drawing of the 4f imaging system used to pump the $YBa_2Cu_3O_7$ disc pattern selectively.

A metallic mask is used to shape the pump beam. This mask is produced by depositing a 300 nm thick aluminum thin film on a glass substrate, transparent to the 400 nm optical pump pulse. We then wet-etched a disc shape on the Al film using a laser lithography process based on an AZ1512 photoresist mask. After exposure and development, the sample was wet etched using a commercial etchant solution for Al (TechniEtch Al-80 from MicroChemicals GmbH). After etching, the residual photoresist was removed using acetone and

isopropanol. The optical pump, propagating through the disc patterned into the Al film, was then imaged onto the sample using a 4f optical system. As the pump matches precisely the shape of the opaque $YBa_2Cu_3O_7$ sample, the GaP detector (Fig. 2) and the Bi:LIGG sample (Fig. 3) are fully shielded from the pump pulses. This aspect is important to avoid possible undesired crosstalk between the pump and probe (see also Supplementary Information S12).

S12. Absence of Pump-induced Magnetic Field Changes Above T_c

We repeated the experiments in Fig. 2 and 3 of the Main Text at 100 K, above the superconducting transition temperature T_c of the $YBa_2Cu_3O_7$ sample.

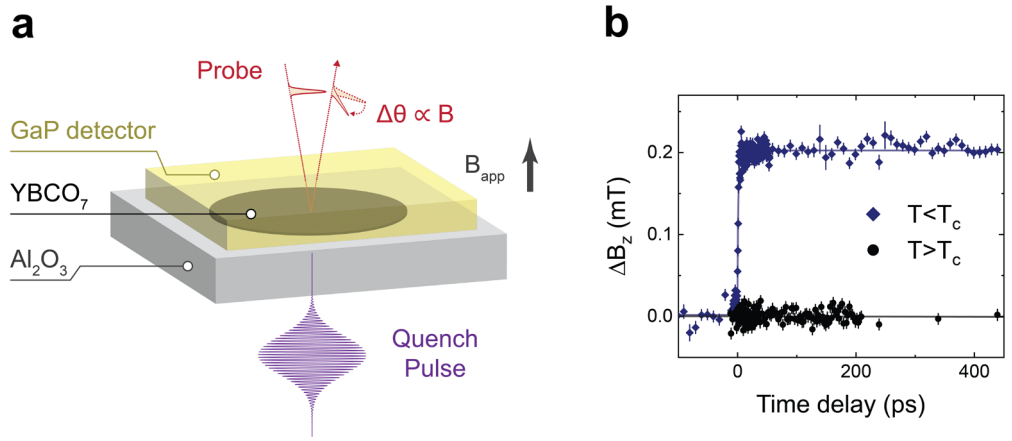

Figure S12.1 | **(a)** Geometry of the experiment. **(b)** Measured magnetic field above the centre of the superconducting disc below T_c at 55 K (blue diamonds) and above T_c at 100 K (black circles) in the GaP detector. Each data point represents the mean value ± s.e.m. extracted from a sample of 1100 and 2200 acquisitions (Supplementary Information S5) for the measurement below and above T_c, respectively.

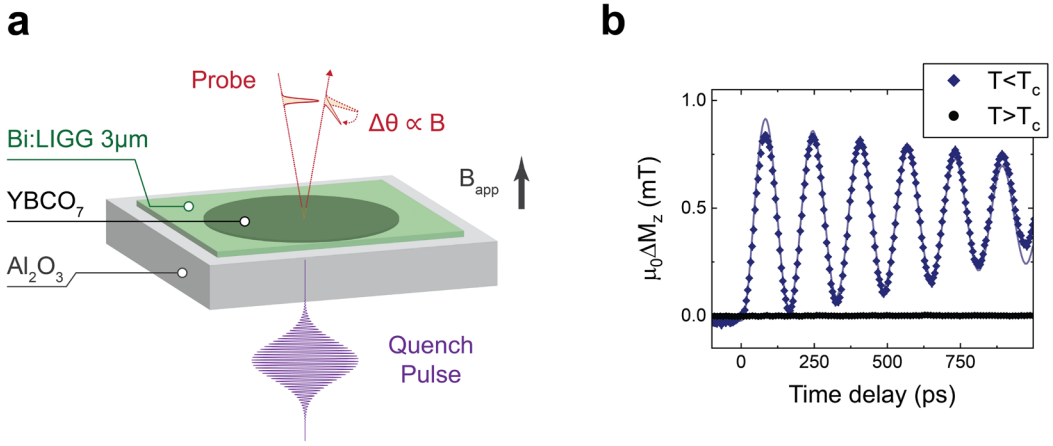

Figure S12.2 | **(a)** Geometry of the experiment. **(b)** Measured magnetic field above the centre of the superconducting disc below T_c at 55 K (blue diamonds) and above T_c at 100 K (black circles) in Bi:LIGG.

Each data point represents the mean value ± s.e.m. extracted from a sample of 360 and 400 acquisitions (Supplementary Information S5) for the measurement below and above T_c, respectively.

The results of this measurement for the GaP detector and the Bi:LIGG sample are indicated by the black dots in Fig. S12.1 and S12.2, respectively. The blue diamonds show the corresponding measurements' results in the same conditions below T_c. The magnetic response disappears above T_c, confirming the magnetic nature of the signal measured and ruling out possible spurious pump-probe effects induced by the optical pump.

S13. Fluence dependence of the Ultrafast Magnetic Step

Fig. S13 shows the measured magnetic field steps for different values of the incident pump fluence.

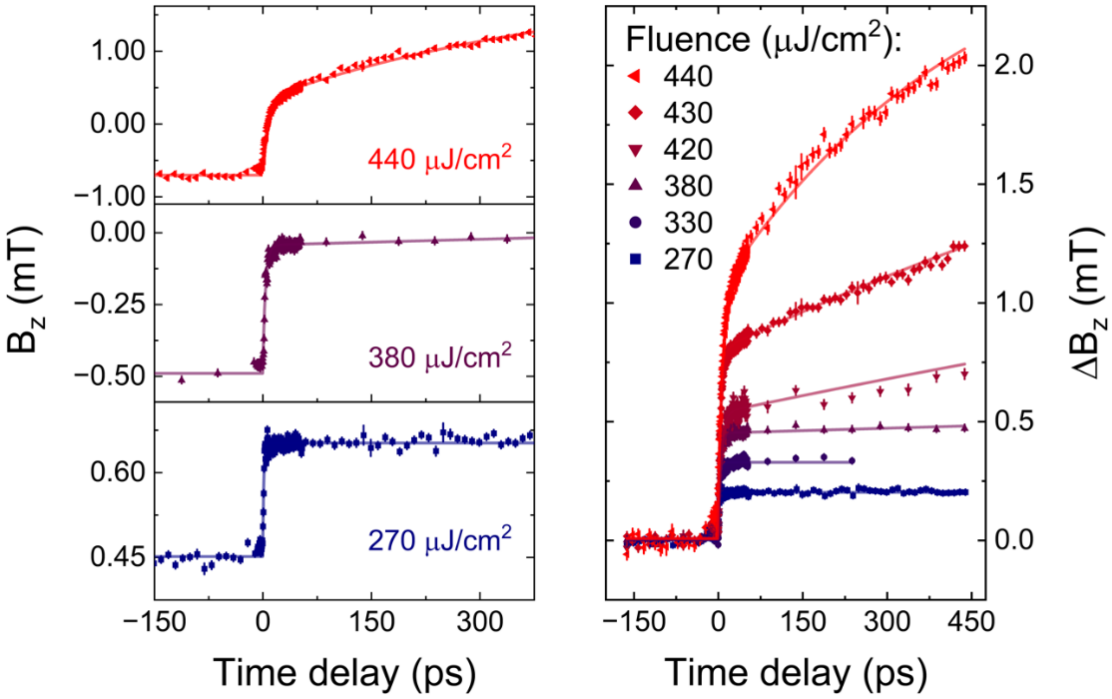

Figure S13. | Experimental data showing the measured magnetic field for three selected fluences of the quench beam (left panel) and the magnetic field changes for six different quench fluences (right panel) versus pump-probe delay. These data have been measured using a GaP magneto-optic detector in the configuration shown in Fig. 2 of the Main Text. Each data point represents the mean value ± s.e.m. extracted from a sample of 1100, 230, 670, 100, 680, and 100 acquisitions (Supplementary Information S5) for the measurements done at a fluence of 270, 330, 380, 420, 430, and 440 μJ/cm², respectively.

The curve measured at the lowest fluence (270 μJ/cm^2) is the same as in Fig. 2 of the Main Text. As we progressively increase the fluence of the pump, the amplitude of the ultrafast magnetic step also increases. The step suddenly changes its behavior at a fluence of ~400 μJ/cm^2, and an additional, slower time scale appears. As discussed in Supplementary Information S14, the curves taken at higher fluence show the presence of trapped flux with opposite polarity at negative time delays. This fact is visible in the negative pump-probe time delay region of the first two graphs (440 and 380 μJ/cm^2) in the left-hand-side panel of Fig. S13.

Averitt et al.[12] performed experiments at 50–100 μJ/cm^2 fluence in 50 nm thick films. In this excitation range, the superconductivity is strongly perturbed and the sample is driven almost to its normal state.

The penetration depth of the 400 nm quench pulse (~100 nm from reference [17]) is approximately the same as that for 800 nm pulses used by Averitt et al.[12]. Given an exponential decay of the quench pulse, as our measurement probes the magnetic signal arising from the whole thickness of the YBCO film, which is 3 times thicker than in reference [12], we expect to observe for the same fluence a significantly smaller perturbation.

This expectation is met in our measurements, where with a fluence of ~270 μJ/cm^2 we achieve only a partial disruption of the superconductor as observed by reduced amplitude of the magnetic step compared to the applied field of 2 mT (see Fig. S13). As the fluence is increased further, the disrupted thickness grows yielding a larger magnetic step.

S14. Pump Induced Magnetic Field Dynamics at Long Time Scales

Fig. S14.1 illustrates the dynamics of the magnetic field around the superconductor assuming that the energy of the quench pulses is enough to fully disrupt superconductivity throughout the sample. Before the first quench pulse arrives, the sample is kept below T_c. The magnetic field above the center of the superconductor is equal to zero, as discussed in Supplementary Information S6.

When the first quench pulse hits the sample, the magnetic field above the center of the superconductor suddenly reaches the value of the external magnetic field, creating an ultrafast magnetic field step. The sample then recovers in an applied magnetic field, which is almost fully trapped within its defects (see Supplementary Information S7).

After that, superconducting screening currents can build up to shield further changes of the applied field and keep the value of the magnetic flux threading the sample constant

(as prescribed by Faraday law) until the next pump pulse disrupts superconductivity again. Importantly, at negative delays, i.e., right before a quench pulse hits the sample, the trapped magnetic flux *can* have a polarity opposite to the applied field. This can also lead to the magnetic step having an amplitude bigger (up to twice) than the amplitude of the external applied field (as hinted by the curves at highest fluence in Fig. S13).

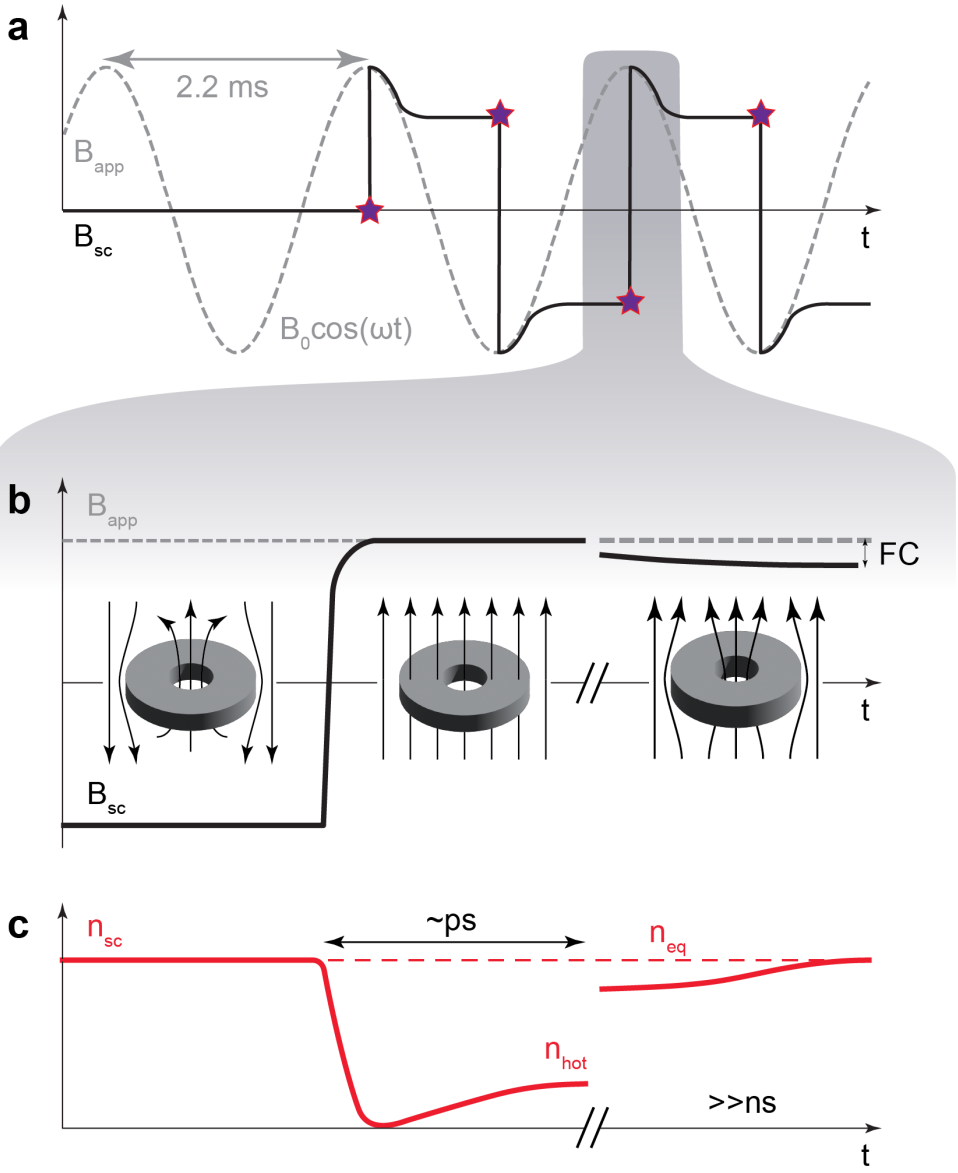

Figure S14.1. (a) Externally applied magnetic field (dashed grey line) and magnetic field in the center of the superconductor (solid black curve). The star indicates the time at which the sample is struck by the quench pulse. **(b)** Zoomed in view of the magnetic field dynamics around the arrival time of the quench pulse. The sketches show an exemplary field line distribution around the sample. The hole represents a non-superconducting defect. After the superconductor recovers, a small field-cooled response occurs (exaggerated in the sketch). We do not detect this contribution in our experiments. **(c)** Time dependence of the superconducting response (see Supplementary Information S9).

Consequences on the Measured Magnetic Signal

Fig. S14.2 builds upon the concepts introduced in Fig. S14.1, incorporating details on how the measured signal is defined (see Supplementary Information S5). The figure provides a schematic representation of how the relative arrival time between the quench and probe pulses influences the measured magnetic signal. This is illustrated for negative time delays (left panel) and positive time delays (right panel). As the measured quantity is defined as the difference in polarization rotation between the positive and negative polarities of the applied magnetic field (see Supplementary Information S5), the measured magnetic field at negative pump-probe delays *can* be negative in our measurements, as shown in Fig. S13. At positive time delays, the value of the magnetic field measured in the vicinity of the sample is positive and close to the value of the externally applied field as observed at long pump-probe delays in the data taken at the highest fluence in Fig. S13.

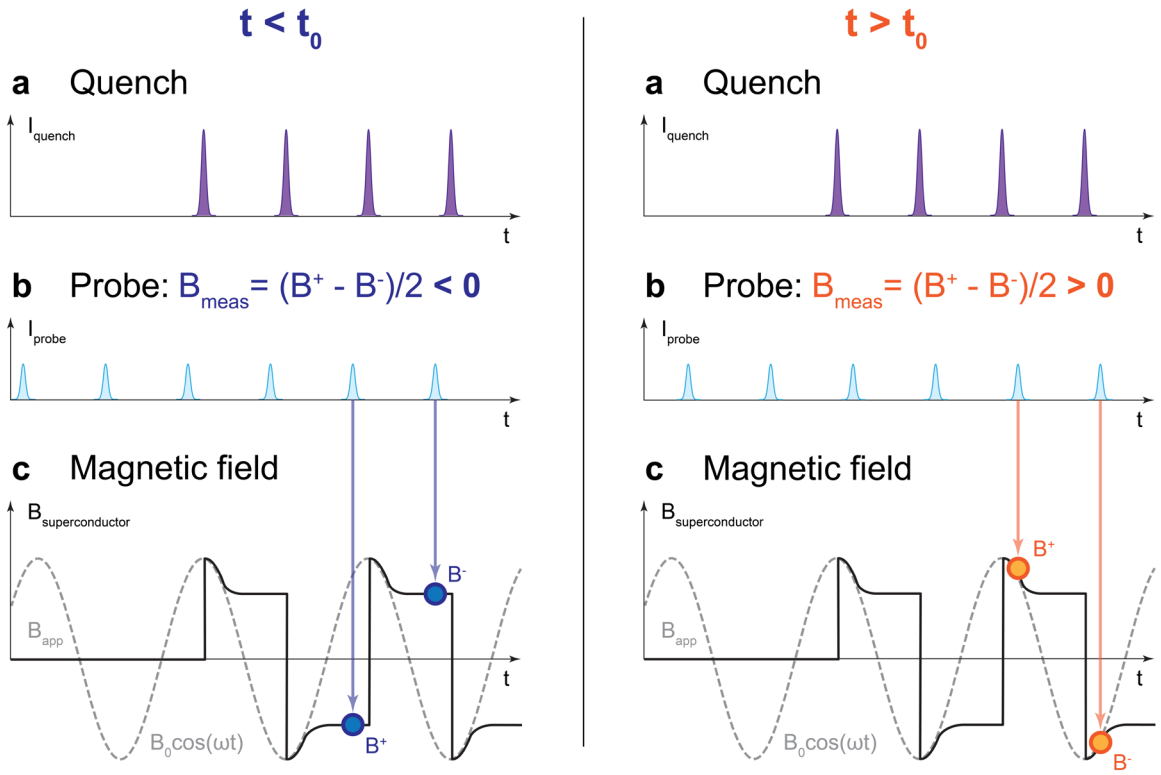

Figure S14.2. | (a) Arrival time of the quench pulses disrupting superconductivity in the sample (same in both the left and the right panels). **(b)** Probe pulses sampling the magnetic field. In the left panel, the probe pulses arrive *before* the arrival time of the respective quench pulses (t_0). The magnetic field measured is negative due to trapped flux with a polarity opposite to the externally applied field. In the right panel, the probe pulses arrive *after* the respective quench pulses ($t>t_0$). The magnetic field measured is positive and close to the value of the externally applied field. **(c)** Externally applied magnetic field (dashed grey line) and magnetic field in the center of the superconductor (solid black curve).

Lifting the complete disruption assumption

To provide a clearer understanding of the data presented in the Main Text, we need to relax the previous assumption that the quench pulse completely disrupts the shielding currents in the sample. Additionally, we must consider that the measured polarization rotation stems from an average throughout the detector volume (see Supplementary Information S1, S8, and Fig. S8.a). The interplay of these two factors leads to the magnetic dynamics illustrated in Fig. S14.3. Here, due to the reduced energy of the quench pulse, residual shielding persists in the deeper layers of the sample. Therefore, the magnetic field following the quench does not reach the external field strength, resulting in a magnetic step of lower amplitude. Moreover, the trapped flux with negative polarity at negative time delays is countered by the applied field, producing a positive signal after averaging through the volume of the magnetic detector traversed by the probe. This framework qualitatively accounts for the results depicted in Fig. 2b of the Main Text.

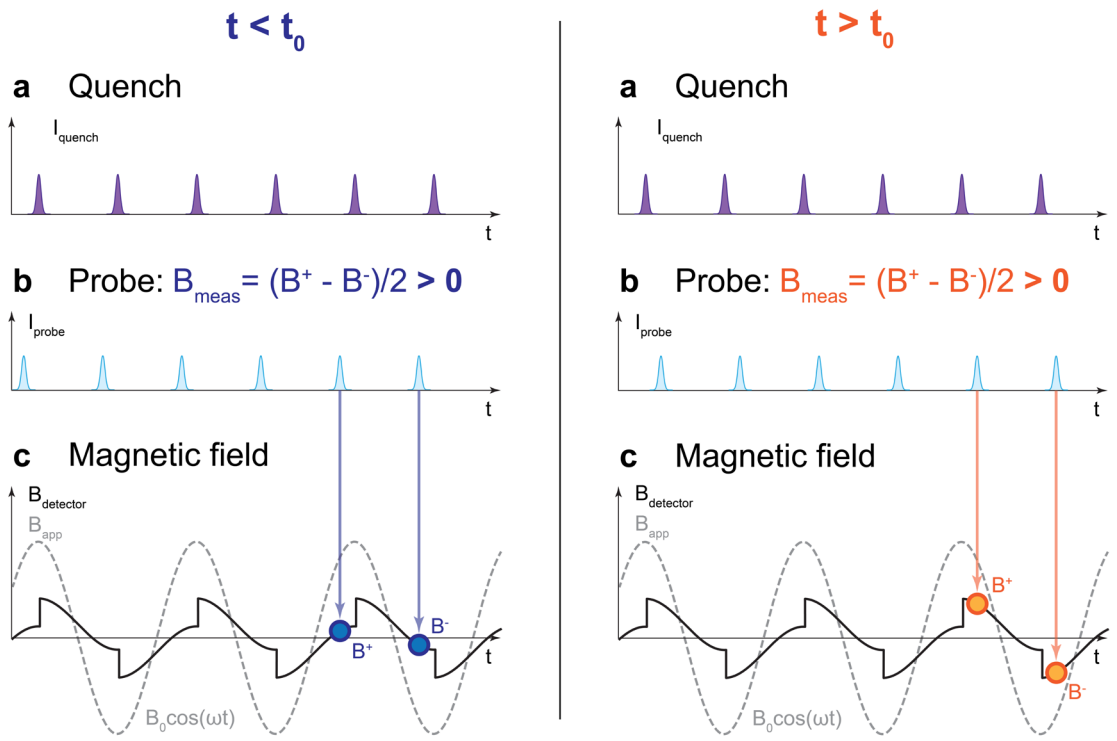

Figure S14.3. | **(a)** Arrival time of the low fluence quench pulses disrupting superconductivity in the sample (same in both the left and the right panels). **(b)** Probe pulses sampling the magnetic field. In the left panel, the probe pulses arrive *before* the arrival time of the respective quench pulses (t_0). At this specific fluence, the magnetic field measured is still positive as the trapped flux with opposite polarity is offset by the applied field. In the right panel, the probe pulses arrive *after* the respective quench pulses ($t>t_0$). The magnetic field measured is positive but not as big as the external field due to the only partial quench of superconductivity. **(c)** Externally applied magnetic field (dashed grey line) and magnetic field at the detector position above the center of the superconductor (solid black curve).

Proposed Method for nulling the residual trapped flux

Finally, we present in Fig. S14.4 a possible alternative measurement protocol to avoid the presence of trapped flux at negative time delays. Here, we assume that the quench pulses deposit enough energy on the sample to completely disrupt superconductivity, and we apply a piecewise sinusoidal external magnetic field as shown by the dashed line in Fig. S14.4c. In this way, we can use half of the quench pulses to "reset" the magnetic field of the superconductor to zero by quenching superconductivity in a zero-applied magnetic field. The field is then measured with probe pulses arriving at half the repetition rate of the quench pulses (Fig. S14.4b). In this way, the field above the superconductor will be zero at negative time delays.

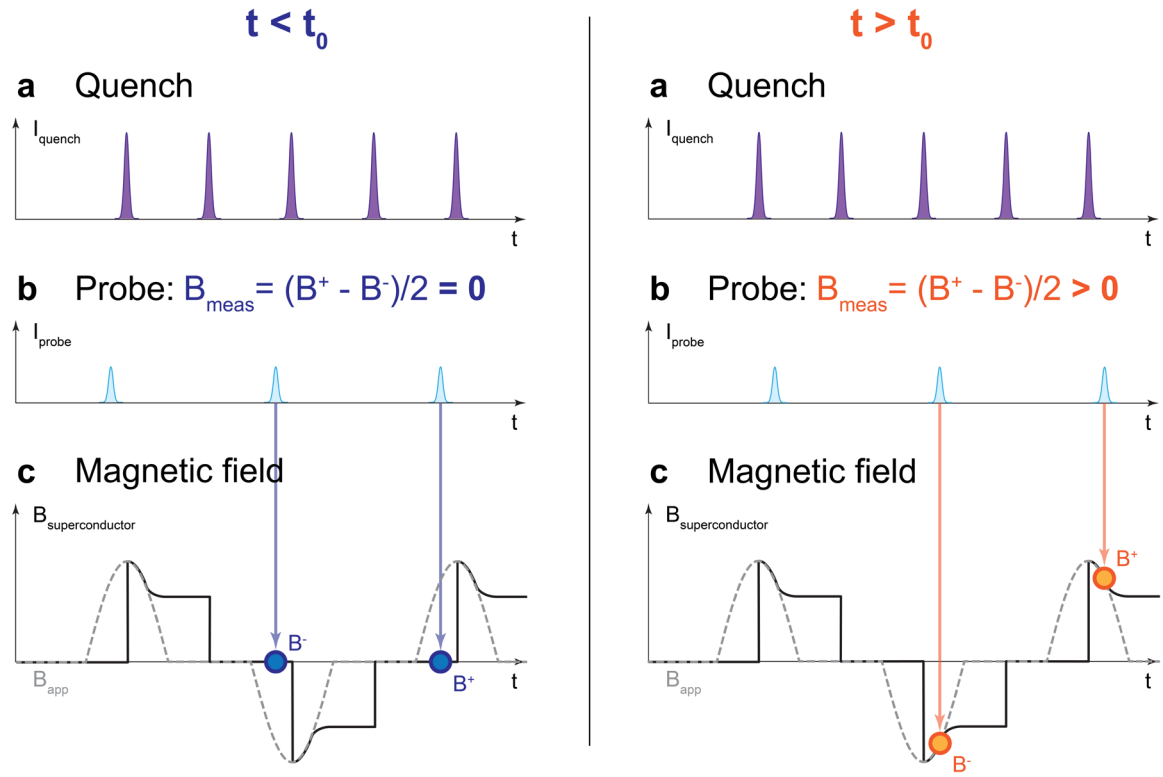

Figure S14.4. | **(a)** Arrival time of the quench pulses disrupting superconductivity in the sample (same in both the left and the right panels). **(b)** Probe pulses sampling the magnetic field at half the repetition rate of the quench pulse. In the left panel, the probe pulses arrive *before* the arrival time of the respective quench pulses ($t<t_0$), and the magnetic field at negative time delays is equal to zero with this experimental scheme. In the right panel, the probe pulses arrive *after* the respective quench pulses ($t>t_0$), and the magnetic field measured is positive and close to the value of the external applied field. **(c)** External applied magnetic field (dashed grey line) and magnetic field in the center of the superconductor (solid black curve).

S15. Fitting the oscillations in Bi:LIGG

The magnetic oscillations shown in Fig. 3 of the Main Text were fitted using the LLG equation capturing the damped magnetic oscillations observed in the data (see Fig. S15):

$$\frac{d\boldsymbol{M}(t)}{dt} = -\gamma \cdot \boldsymbol{M}(t) \times \boldsymbol{H}_{eff}(t) + \frac{\alpha}{M_s} \cdot M(t) \times \frac{d\boldsymbol{M}(t)}{dt} \qquad \text{(Eq. S15)}$$

where: t is the independent variable representing the time-delay, **M**(t) represents the time-dependent magnetization inside the material triggered by the quench of the effective field $\mathbf{H}_{\text{eff}}(t)$ when superconductivity in the thin film is disrupted, γ is the gyromagnetic ratio of the electron, α represents the Gilbert damping and the saturation magnetization of the material (quantities written in bold character represent vector quantities). The effective field $\mathbf{H}_{\text{eff}}(t)$ is the sum of two orthogonal components: a static contribution accounting for the magnetic anisotropy (as described below) and a dynamic out-of-plane contribution given by the magnetic step.

In our model the magnetocrystalline anisotropy is neglected, as it is expected to be significantly smaller than shape anisotropy. This is due to the demagnetizing factor of the Bi:LIGG thin film sample, which approaches 1 along the out-of-plane direction[18,19]. Consequently, the out-of-plane direction becomes a hard axis for the magnetization. This behavior can be described by a shape anisotropy energy term: $E_{shape} = \frac{1}{2}\mu_0 M^2 \cos^2(\theta)$, where θ is the angle between the film normal and the magnetization vector M (see, for instance, Blundell chapter 6 paragraph 7.2 [19]). When no external magnetic field is applied, the magnetization naturally lies within the plane of the film. A perpendicular field causes the magnetization to rotate out of the plane. For small out-of-plane rotations ($\theta \sim \frac{\pi}{2} + \varepsilon$, with $\varepsilon \ll 1$) the shape anisotropy energy term E_{shape} can be modeled as an effective magnetic field lying in the plane of the film. This field points along the equilibrium magnetization direction and has a magnitude equal to the magnetization itself. The corresponding energy term is: $E_{eff} = -M \cdot H_{eff} = -\mu_0 M^2 \cos(\frac{\pi}{2} - \theta)$, where θ is defined as above. Substituting $\theta \sim \frac{\pi}{2} + \varepsilon$ we find: $E_{eff} = -\mu_0 M^2 \cos(\varepsilon) \sim -\mu_0 M^2 + \frac{1}{2}\mu_0 M^2 \varepsilon^2$. Similarly, the shape anisotropy energy can be expressed as: $E_{shape} = \frac{1}{2}\mu_0 M^2 \cos^2(\frac{\pi}{2} + \varepsilon) = \frac{1}{2}\mu_0 M^2 \sin^2(\varepsilon) \sim \frac{1}{2}\mu_0 M^2 \varepsilon^2$. Thus, a part from a constant energy offset, the two energy terms share the same functional form. Consequently, they produce the same force on the

sample magnetization in the LLG equation. Note that, the small angle approximation invoked above is justified since the amplitude of the applied field is at most 3 mT while M_s~220mT. Hence, the angular deviation ε is smaller than ~1°.

The dynamic out-of-plane contribution is modelled using the temporal profile of the magnetic transient measured in GaP (see Fig. 2) scaled to an amplitude of ~0.6 mT. We then compare the time evolution of the simulated magnetization z-component with the measured magnetization in the Bi:LIGG sample. The fit shown in Fig. 4 (also reported in Fig. S15 below, for convenience) is achieved by varying the saturation magnetization M_s of the Bi:LIGG sample and the value of the Gilbert damping α. The obtained values are M_s~220mT and α~0.014. The saturation magnetisation value agrees well with other literature values measured for rare earth substituted bismuth iron garnets.

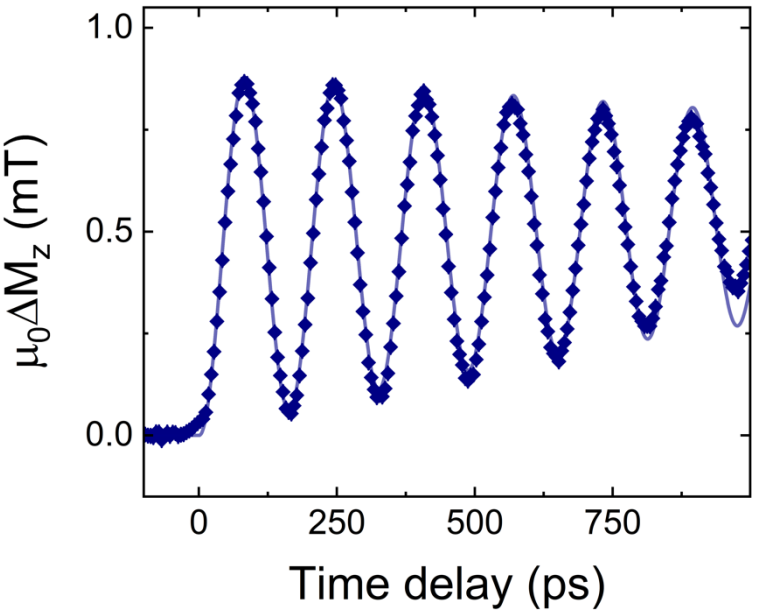

Figure S15. | Fit of the time-dependent changes in the z-component of the magnetization ΔM_z of Bi:LIGG, measured above the centre of the superconducting disc as a function of quench-probe delay. The value of the z-component of the magnetization at negative time delays is equal to -1.375 mT due to negative trapped flux before the pump pulse hits the sample (see Supplementary Information S14). Each data point represents mean value ± s.e.m. (smaller than the size of the data points) extracted from a sample of 360 acquisitions (Supplementary Information S5).

References (Supplementary Information)

1. Goa, P. E., Hauglin, H., Olsen, Å. A. F., Baziljevich, M. & Johansen, T. H. Magneto-optical imaging setup for single vortex observation. *Rev. Sci. Instrum.* **74**, 141–146 (2003).
2. Koblischka, M. R. & Wijngaarden, R. J. Magneto-optical investigations of superconductors. *Supercond. Sci. Technol.* **8**, 199 (1995).
3. Riordan, J. A., Lu, Z. G. & Zhang, X.-C. Free-Space Ultrafast Magneto-Optic Sampling. in *Conference on Lasers and Electro-Optics (1997), paper CPD10* CPD10 (Optica Publishing Group, 1997).
4. Riordan, J. A. & Zhang, X.-C. Sampling of free-space magnetic pulses. *Opt. Quantum Electron.* **32**, 489–502 (2000).
5. Parsons, D. F. & Coleman, P. D. Far Infrared Optical Constants of Gallium Phosphide. *Appl. Opt.* **10**, 1683_1-1685 (1971).
6. Lee, W. C. & Johnston, D. C. Superconducting and normal-state magnetic-susceptibility anisotropy in $YBa_2Cu_3O_7$. *Phys. Rev. B* **41**, 1904–1909 (1990).
7. Tinkham, M. *Introduction to Superconductivity*. (Courier Corporation, 2004).
8. Liang, R., Dosanjh, P., Bonn, D. A., Hardy, W. N. & Berlinsky, A. J. Lower critical fields in an ellipsoid-shaped $YBa_2Cu_3O_{6.95}$ single crystal. *Phys. Rev. B* **50**, 4212–4215 (1994).
9. Brandt, E. H. Geometric edge barrier in the Shubnikov phase of type-II superconductors. *Low Temp. Phys.* **27**, 723–731 (2001).
10. Prozorov, R. Meissner-London Susceptibility of Superconducting Right Circular Cylinders in an Axial Magnetic Field. *Phys. Rev. Appl.* **16**, 024014 (2021).
11. Brandt, E. H. & Indenbom, M. Type-II-superconductor strip with current in a perpendicular magnetic field. *Phys. Rev. B* **48**, 12893–12906 (1993).

12. Averitt, R. D. *et al.* Nonequilibrium superconductivity and quasiparticle dynamics in $YBa_2Cu_3O_{7-\delta}$. *Phys. Rev. B* **63**, 140502 (2001).
13. Kaindl, R. A. *et al.* Ultrafast Mid-Infrared Response of $YBa_2Cu_3O_{7-\delta}$. *Science* **287**, 470–473 (2000).
14. Pashkin, A. *et al.* Femtosecond Response of Quasiparticles and Phonons in Superconducting $YBa_2Cu_3O_{7-\delta}$ Studied by Wideband Terahertz Spectroscopy. *Phys. Rev. Lett.* **105**, 067001 (2010).
15. Kabanov, V. V., Demsar, J., Podobnik, B. & Mihailovic, D. Quasiparticle relaxation dynamics in superconductors with different gap structures: Theory and experiments on $YBa_2Cu_3O_{7-\delta}$. *Phys. Rev. B* **59**, 1497–1506 (1999).
16. Winzer, K. & Kumm, G. Fluctuation-enhanced conductivity and magnetoconductivity of high-quality $YBa_2Cu_3O_{7-\delta}$ crystals. *Z. Für Phys. B Condens. Matter* **82**, 317–321 (1991).
17. Lee, Y. S. Electrodynamics of the nodal metal state in weakly doped high-T_c cuprates. *Phys. Rev. B* **72**, (2005).
18. Charles Kittel. Introduction to Solid State Physics. 8th Edition. Wiley. *Wiley.com*.
19. Blundell, S. *Magnetism in Condensed Matter*. (Oxford University Press, Oxford, New York, 2001).